# Extreme sensitivity of crosshole Electrical Resistivity Tomography measurements to geometric errors

Paul B. Wilkinson, Jonathan E. Chambers, Mike Lelliott, Gary P. Wealthall, and Richard D. Ogilvy.

British Geological Survey, Natural Environment Research Council, Kingsley Dunham Centre, Keyworth, Nottingham, NG12 5GG, UK

Accepted 2008 January 9. Received 2008 January; in original form 2007 June 18

(Short title: Extreme geometric errors in crosshole ERT)

Corresponding Author: Paul Wilkinson, Tel: +44(0) 115 936 3086

Fax: +44(0) 115 936 3261. Email: pbw@bgs.ac.uk

*Geophysical Journal International* (2008) **173**, 49-62
http://www.blackwell-synergy.com/doi/pdf/10.1111/j.1365-246X.2008.03725.x

# Summary

The effects of geometric errors on crosshole resistivity data are investigated using analytical methods. Geometric errors are systematic and can occur due to uncertainties in the individual electrode positions, the vertical spacing between electrodes in the same borehole, or the vertical offset between electrodes in opposite boreholes. An estimate of the sensitivity to geometric error is calculated for each of two generic types of four-electrode crosshole configuration: current flow and potential difference crosshole (XH) and in-hole (IH). It is found that XH configurations are not particularly sensitive to geometric error unless the boreholes are closely spaced on the scale of the vertical separation of the current and potential electrodes. But extremely sensitive IH configurations are shown to exist for any borehole separation. Therefore it is recommended that XH configurations be used in preference to IH schemes. The effects of geometric error are demonstrated using real XH data from a closely spaced line of boreholes designed to monitor bioremediation of chlorinated solvents at an industrial site. A small fraction of the data had physically unrealistic apparent resistivities, which were either negative or unexpectedly large. But by filtering out configurations with high sensitivities to geometric error, all of the suspect data were removed. This filtering also significantly improved the convergence between the predicted and the measured resistivities when the data were inverted. In addition to systematic geometric errors, the measured data also exhibit a high level of random noise. Despite this, the resulting inverted images correspond reasonably closely with the known geology and nearby cone penetrometer resistivity profiles.

# Keywords

Electrical resistivity, Borehole, Tomography, Inversion, Sensitivity

# 1. Introduction

Volumetric imaging of the electrical properties of the subsurface by electrical resistivity tomography (ERT) has been intensively developed for over a decade. Permanently installed electrode arrays can now be used with automated multi-channel data acquisition systems and rapid inversion algorithms to enable 2D or 3D time-lapse imaging of dynamic processes (Versteeg *et al.* 2004; LaBreque *et al.* 2004; Ogilvy *et al.* 2007). As the capabilities of such systems increase, more electrodes can be used thereby potentially increasing the spatial resolution of the resulting images. However, the resolution is not only limited by the separation of the electrodes, but also by errors affecting the data (LaBrecque *et al.* 1996). An often-overlooked source of error in geoelectrical imaging is uncertainty in the geometry of the array, which can include errors in the position or spacing of the electrodes, or in the relative offset between adjacent arrays. However, in the closely related technique of medical Electrical Impedance Tomography (EIT) this problem has been known for several years. This is partly because the EIT electrodes tend to be closely spaced due to the size of the body and the need for high-resolution images (Blott *et al.* 1998). But it is also important because electrodes attached to certain parts of the body (e.g. the chest) will move during imaging (Zhang & Patterson 2005). Indeed, recent improvements to medical EIT inversion algorithms treat the electrode positions in the same way as the impedance distribution; they are unknown model parameters to be determined from the data and the a priori constraints (Soleimani *et al.* 2006).

In geoelectrical imaging, it is usually reasonable to assume that the electrode locations will remain constant over time. But configurations with small electrode spacings could be prone to significant errors due to uncertainties in those locations. This could be more of an issue for subsurface than surface electrodes, since the positions of the latter are much easier to check. As the use of site-scale crosshole ERT imaging is becoming more common in engineering and environmental investigations (Ramirez *et al.* 1996; Daily & Ramirez 2000; Slater & Binley 2003; Goes & Meekes 2004; LaBreque *et al.* 2004; Wilkinson *et al.* 2006; Chambers *et al.* 2007), the incidence of data affected by geometric errors is likely to increase. To our knowledge, there have only been two detailed studies of the effects of this type of error on resistivity data. Zhou & Dahlin (2003) discuss the effect of such errors on the geometric factors of commonly used 2D surface ERT arrays. Using heterogeneous synthetic forward models, they found that the relative error in the observed apparent resistivity can be more than double the relative electrode spacing error for certain configurations. Oldenborger *et al.* (2005) studied the effects of electrode mislocation on synthetic crosshole ERT data for pole-pole and bipole-bipole configurations (either vertical bipoles of 1 m length, or horizontal bipoles of 6 m length). They found that large errors in resistivity (~50 % for a 10 cm position error) could occur depending on the relative positions and orientation of the bipoles (either horizontal or vertical). They also found that the statistical distribution of errors was complicated and multi-modal and could introduce bias into the measured data sets.

In this paper, we take an approach similar to that of Zhou & Dahlin (2003) to calculate an estimate of the sensitivity to geometric error of any inter-borehole four-electrode ERT configuration that falls into one of two generic types. These types encompass and extend the bipole-bipole configurations studied by Oldenborger *et al.* (2005), and our findings support and complement theirs. Rather than repeating their synthetic modelling, we demonstrate the efficacy of our approach using real crosshole ERT data from a “transect borehole array”, a line of seven closely spaced boreholes that has been installed to monitor resistivity changes associated with the bioremediation of a contaminated site. Following the suggestion of Oldenborger *et al.* (2005), we use the estimates of geometric error sensitivity in our processing and inversion procedure to remove highly sensitive measurements from the data set. We demonstrate that this removes all the outlying data points with negative or suspiciously large apparent resistivities. After removal of the outlying data, the tomographic images from individual panels (pairs of boreholes) and the whole transect show significant improvements in the RMS misfits between the inverted and measured data.

## 2. Electrode array geometric errors

To assess the sensitivity of inter-borehole resistivity measurements to geometric errors, we categorize the commonly used four-electrode measurements into two basic types (Bing & Greenhalgh 2000); those for which the current flow and potential measurements are crosshole (XH, see Figs. 1(a) and (c)) or in-hole (IH, see Figs. 1(b) and (d)). Of the two types, XH configurations provide greater image resolution in the region between the boreholes, and tend to offer better signal-to-noise characteristics (Bing & Greenhalgh 2000; Wilkinson *et al.* 2006; Chambers *et al.*

2007). For these reasons research into the use of crosshole ERT is starting to favor XH over IH configurations, e.g. compare Slater & Binley (2003) with Slater *et al.* (2002).

Depending on the method of installation of the borehole electrodes, errors in the geometry may be general (i.e. all four electrodes have uncertain positions), spacing related (e.g. imprecise spacings between electrodes in the same borehole), or offset related (e.g. spacings are known to high precision, but the depths of arrays in adjacent boreholes are uncertain). Figure 1 illustrates the general case, and also the case of uncertain offsets between adjacent boreholes, which affects the data that is presented in this paper. The general case is shown for XH and IH measurements in Figs. 1(a) and 1(b) respectively. The current electrodes (labelled A and B) are located at depths $\alpha$ and $\beta$, and the potential electrodes (M and N) are at depths $\mu$ and $v$. Each of the four depths is imprecisely known. The effect of errors in the electrode depths on the apparent resistivity is calculated from the geometric factor $K$. This is given by

$$K = \frac{4\pi}{\dfrac{1}{r_{\mathrm{AM}}} - \dfrac{1}{r_{\mathrm{AN}}} - \dfrac{1}{r_{\mathrm{BM}}} + \dfrac{1}{r_{\mathrm{BN}}} + \dfrac{1}{r_{\mathrm{A'M}}} - \dfrac{1}{r_{\mathrm{A'N}}} - \dfrac{1}{r_{\mathrm{B'M}}} + \dfrac{1}{r_{\mathrm{B'N}}}}, \qquad (1)$$

where, for example, $r_{\mathrm{AM}}$ is the distance between A and M. A′ and B′ represent the locations of the images of the current electrodes A and B respectively. If the location of A is $(x_{\mathrm{A}}, y_{\mathrm{A}}, z_{\mathrm{A}})$, then A′ is at $(x_{\mathrm{A}}, y_{\mathrm{A}}, -z_{\mathrm{A}})$, assuming that the ground surface is $z = 0$. The systematic error in $K$ due to uncertainty in the depths depends on the partial derivatives $(\partial K/\partial\alpha)$, $(\partial K/\partial\beta)$, $(\partial K/\partial\mu)$ and $(\partial K/\partial v)$ where, for example,

$$\frac{\partial K}{\partial \alpha} = \frac{\partial K}{\partial r_{\mathrm{AM}}}\frac{\partial r_{\mathrm{AM}}}{\partial \alpha} + \frac{\partial K}{\partial r_{\mathrm{AN}}}\frac{\partial r_{\mathrm{AN}}}{\partial \alpha} + \frac{\partial K}{\partial r_{\mathrm{A'M}}}\frac{\partial r_{\mathrm{A'M}}}{\partial \alpha} + \frac{\partial K}{\partial r_{\mathrm{A'N}}}\frac{\partial r_{\mathrm{A'N}}}{\partial \alpha}. \qquad (2)$$

Note that for ($\partial K/\partial\alpha$), all partial derivatives of distances involving electrode B are zero and have been left out of Eq. 2. Similar simplifications apply for ($\partial K/\partial\beta$), ($\partial K/\partial\mu$) and ($\partial K/\partial\nu$). Assuming that the errors $\Delta\alpha$, $\Delta\beta$, $\Delta\mu$ and $\Delta\nu$ are independent and uncorrelated then an estimate of the error in $K$, $\Delta K$, is given by Gaussian error propagation as

$$\Delta K^2 = \left(\frac{\partial K}{\partial\alpha}\right)^2 \Delta\alpha^2 + \left(\frac{\partial K}{\partial\beta}\right)^2 \Delta\beta^2 + \left(\frac{\partial K}{\partial\mu}\right)^2 \Delta\mu^2 + \left(\frac{\partial K}{\partial\nu}\right)^2 \Delta\nu^2 . \tag{3}$$

In ERT inversion it is usually the relative error in the apparent resistivity, $\rho_a$, that is used in the merit function to test for convergence. It is also often the case that logarithms of the resistivity data are used to improve the stability of the inversion by transforming the typically large resistivity range to a linear scale. If so, then the relative error also appears in the data discrepancy vector (Loke & Barker 1995) since $\Delta\ln(\rho_a) = \Delta\rho_a/\rho_a$. This ensures that the apparent resistivity data all have equal weight, whatever their magnitude. For these reasons, relative rather than absolute errors are also used throughout this paper. Since $\rho_a = KV/I$, where $V$ is the measured voltage and $I$ is the applied current, then the relative error in the apparent resistivity due to a systematic error in $K$ is

$$\frac{\Delta\rho_a}{\rho_a} = \frac{\Delta K}{K} . \tag{4}$$

Before we consider specific cases, it is worth noting that the preceding analysis is not limited to four-electrode configurations; it can be applied to any configuration with any number of electrodes providing that their positions are independent. In certain situations, however, the errors in some electrode positions may be correlated. One such case is where electrodes are fixed to a rigid structure prior to deployment in the borehole. In this case, the errors in the vertical electrode spacings are negligible in comparison with the errors in the depths to which each array is installed. Therefore the spacing errors can be neglected, leaving only errors in the two independent depths of installation. Since this arrangement was used to collect the data that is presented later in this paper, we examine it here in detail for a range of borehole separations and electrode depths in both XH and IH configurations. We assume for now that the electrodes in each hole have the same vertical separation $a$, and express the other distances in the problem as multiples of $a$ (see Figs. 1(c) and 1(d)). The inter-borehole separation is $\delta a$, and the midpoint depths of the electrodes in the left- and right-hand boreholes are $\gamma a$, and $\varepsilon a$ respectively. To illustrate the dependence of $\Delta K/K$ on borehole separation and midpoint depth, we calculate the related quantity $\sigma/K$ where

$$\sigma = \sqrt{\left(\frac{\partial K}{\partial \gamma}\right)^2 + \left(\frac{\partial K}{\partial \varepsilon}\right)^2} \tag{5}$$

is the estimate of the error in $K$ that would occur for unit errors in $\gamma$ and $\varepsilon$, and $\sigma/K$ is the associated relative error. The reason for assuming constant unit uncertainties in $\gamma$ and $\varepsilon$ is so that we can compare the behaviours of the error estimate for different configurations.

The 3D surface plot in Fig. 2(a) shows $\sigma$ for XH configurations as a function of the borehole separation $\delta$ and the right-hand borehole midpoint depth $\varepsilon$. Below this the 2D plots show the detailed behaviour of $\sigma$ for $\delta = 0.5$, 0.7 and 1.0. For all the plots the range of right-hand midpoint depths is $5 \le \varepsilon \le 15$, and the left-hand midpoint depth is fixed at $\gamma = 10$. Figs. 2(b) and 2(c) show $1/K$ and $\sigma/K$ respectively. For $\delta < 1$, the vertical spacing between the electrodes in the same hole, $a$, is larger than the spacing between the boreholes, $\delta a$. Figure 2(c) shows that large values of $\sigma/K$ can occur in this regime. Consequently, large relative changes in $K$, and hence in $\rho_a$, can occur for small uncertainties in the depths of the arrays ($\gamma$ and $\varepsilon$). For small δ (< ~0.7), $\sigma/K$ can be negative and large enough to cause the apparent resistivity to change sign. Although real negative apparent resistivities are unusual, they can occur when large resistivity contrasts exist in the vicinity of the electrodes (see Appendix A). Therefore the presence of such data can cause inversion algorithms to generate unstable solutions with large abrupt changes in resistivity near electrode locations. However it is usually the case that $\delta > 1$, unless the aspect ratio (borehole separation / borehole depth) is small. Figure 2 shows that XH configurations are not strongly affected by offset errors between adjacent borehole arrays when $\delta > 1$.

For IH configurations Fig. 3 shows (a) $\sigma(\delta, \varepsilon)$, (b) $1/K(\delta, \varepsilon)$, and (c) $\sigma/K(\delta, \varepsilon)$ as surface plots and line plots for $\delta = 0.5$, 1.0 and 1.5. Note that the ordinate axes of all plots in Fig. 3 have larger ranges than in Fig. 2. By contrast with the case for the XH configurations, $1/K$ for the IH configurations can change sign for any borehole separation $\delta$ (Fig. 3(b)). Also, for most combinations of $\delta$ and $\varepsilon$, the error estimate $\sigma$ (Fig. 3(a)) is typically much larger than for XH configurations. Therefore the estimate of the relative error $\sigma/K$ shows that, for *any* borehole separation, there are IH configurations that are extremely sensitive to small uncertainties in array depth. Depending on the exact details of the actual and assumed locations of the electrodes, these configurations could easily return apparent resistivities with the incorrect sign (usually negative).

High sensitivities to geometric error will occur when $K$ is close to a singularity, or equivalently $1/K \approx 0$ (compare Figs. 2(b) and (c), and 3(b) and (c) for examples). To understand why this is, we consider the extreme cases where the sign of the apparent resistivity can change with a small change in the depth of one of the rigid arrays. In general, if the potential electrode M is closer to the current electrode A than it is to B, and similarly N is closer to B than A, then the geometric factor $K > 0$. But if, for example, M moves significantly closer to B than to A, then the geometric factor can change sign ($K < 0$). If we are sufficiently close to this situation, then a small uncertainty in the position of M can cause the calculated magnitude (and sign) of $K$ to be wrong, giving a large error in the apparent resistivity, which may also change sign. This explains why the XH configurations are largely unaffected by geometric errors; if $\delta > 1$ it is not possible for M to be closer to A than it is to B (see Fig. 1(c)). But for IH configurations, there will always be combinations of $\gamma$ and $\varepsilon$ for which M is closer to A than B and vice versa (see Fig. 1(d)). Note that these arguments are rather simplistic since they do not account for the effect of N, nor of the image charges A′ and B′. Nevertheless it is true that, whatever the borehole separation, there will always be IH configurations that will be very sensitive to geometric error, and which should not be used to collect data. Any XH configuration will be safe to use provided that the borehole separation is larger than the vertical spacing between the current and potential electrodes. For this reason, we recommend the use of XH configurations over IH schemes such as skip-1, skip-2, …, skip-*n* (Slater *et al.*, 2002).

## 3. SABRE test site and data collection

The data set that is analyzed in this paper was collected to test a high-density ERT transect array as part of the SABRE (Source Area BioREmediation) project. This project comprises a public / private consortium of twelve companies, two government agencies, and three research institutions. Its charter is to determine if enhanced anaerobic bioremediation can result in effective and quantifiable treatment of chlorinated solvent Dense Non-Aqueous Phase Liquid (DNAPL) source areas. The SABRE research site is located at an operational industrial plant in the UK, within an area contaminated with trichloroethene (TCE). The TCE source zone impacts a shallow unconsolidated aquifer comprising alluvium and river terrace deposits, underlain by mudstones. The water table at the site is between 0.5 m and 0.8 m below ground level. A pilot-scale experimental test cell has been installed at the SABRE site to study the combined effects of biostimulation and bioaugmentation on the biodegradation of TCE.

It is anticipated that ERT will be sensitive to changes in groundwater chemistry associated with the dissolution of DNAPL TCE and its breakdown products, dichloroethene, vinyl chloride and chloride. The SABRE test cell has therefore been instrumented to monitor the enhanced bioremediation experiment using ERT imaging as well as conventional groundwater sampling. Combined ERT and multi-level groundwater sampling arrays have been installed on borehole transects in both the source and plume zones (see Fig. 4). The ERT arrays consist of stainless steel ring electrodes with a vertical separation of 200 mm mounted on a 40 mm diameter plastic tube. The use of ring electrodes can cause systematic artefacts when the data is inverted if the inversion code assumes, as is typically the case, that the electrodes are point-like. It is fairly straightforward to calculate the difference between potentials measured from ring and point electrodes (Ridd 1994); the effect on the various configurations used in this work will be between ~0.5 % and ~3.5 % depending on the vertical electrode separation. This is somewhat smaller than the effects of random noise and geometric uncertainties, which are quantified below. The arrays were installed in 100 mm diameter holes drilled using the sonic percussion drilling method. It is estimated that this method disturbed and compacted the ground in a cylindrical region around each borehole with a diameter of ~200 mm. Figure 4 shows a simplified lithostratigraphic section along the source zone transect, the expected resistivities of each stratum estimated from nearby cone penetrometer resistivity profiles, and an indication of the depths below ground level (bgl) to the base of each borehole. The strata interfaces are approximate since they were interpolated from core logs taken from other boreholes adjacent to the site; the logs from the transect boreholes were not used due to slippages in the core barrels. The locations of the transect boreholes are given in Table 1 (as distances from borehole 44) together with the surveyed elevation of the ground and the depths to which each array was installed. In each borehole, the top few electrodes within the made ground had very high contact resistances and so were not used for resistivity measurements.

The depths of the top functional electrode in each borehole are also shown in Table 1. All depths were measured to an accuracy of ~1 cm.

| Borehole ID | Distance (m) | Surveyed gound elevation (m) | Depth to base of array (mbgl) | Depth of top electrode (mbgl) |
|---|---|---|---|---|
| 44 | 0.00 | 0.000 | 6.71 ± 0.01 | 0.71 ± 0.01 |
| 45 | 0.45 | 0.043 | 6.31 ± 0.01 | 0.71 ± 0.01 |
| 46 | 0.96 | 0.055 | 6.29 ± 0.01 | 0.69 ± 0.01 |
| 47 | 1.48 | 0.009 | 6.02 ± 0.01 | 0.62 ± 0.01 |
| 48 | 1.96 | 0.053 | 6.11 ± 0.01 | 0.91 ± 0.01 |
| 49 | 2.36 | 0.041 | 6.08 ± 0.01 | 0.88 ± 0.01 |
| 50 | 2.74 | 0.018 | 6.38 ± 0.01 | 0.98 ± 0.01 |

**TABLE 1: Locations and depths of borehole arrays.**

Apparent resistivity measurements were made on each panel (adjacent pair of boreholes) using an AGI SuperSting R8 IP system. This is a 200 W, eight-channel instrument, which permits the automated acquisition and storage of up to eight simultaneous apparent resistivity measurements for a given pair of current electrodes. A XH-only measurement scheme was used, which is shown in Fig. 5(a). Current was passed between electrodes A and B, and potential differences were measured between adjacently numbered potential electrodes (i.e. $P_2$-$P_1$, $P_3$-$P_2$, … , $P_9$-$P_8$). A and B started at the base of each borehole (so there could be a significant vertical offset between A and B depending on the differing depths to the bases of the adjacent holes). The eight potential differences were measured, and then A was moved to the position of B, B to $P_1$, $P_1$ to $P_2$ etc, and the process was repeated. This continued until the top of the boreholes was reached. At this point, a similar scheme was used where the potential differences *below* A and B were measured, with A and B moving back down the boreholes. This ensured that each measurement was made twice in reciprocal configurations (Parasnis 1988), with the average of the two measurements being taken as the apparent resistivity for that particular configuration. The same measurement scheme was used for each panel, but the total number of measurements for each panel was different because differing numbers of electrodes were left unused at the tops of the boreholes (see Table 1). In total, there were 2,378 reciprocal data pairs for the whole transect array, comprising 419 for panel 1 (boreholes 44-45), 411 for panel 2 (45-46), 403 for panel 3 (46-47), 387 for panel 4 (47-48), 379 for panel 5 (48-49), and 379 for panel 6 (49-50). The difference between each pair of reciprocal measurements was used as an estimate of its random error to weight the data in the inversion. The full data set of 2,378 measurements had a median reciprocal error of 4.5 %. Note that the error estimated from the reciprocal pair data is due to random noise in the voltage measurement; it is not affected by geometric errors since these are systematic in nature (Oldenborger *et al.* 2005).

## 4. Data processing and inversion

Despite the fact that only XH measurements were used to collect the data, some of the electrode configurations were still highly sensitive to geometric error. This was due to the narrow aspect ratio of the panels and the presence of large vertical offsets between some pairs of adjacent boreholes. To reduce the effect of geometric errors, we calculated the estimated sensitivity of each measurement to this type of uncertainty. The geometry of the XH arrays is defined in Fig. 5(b). Note that the spacing between the current and potential electrodes can be different in each hole, and that the distances $a$, $b$, $c$, $d$, and $e$ are absolute (they are no longer dimensionless multiples of a common distance). We define

$$s = \sqrt{\left(\frac{\partial K}{\partial c}\right)^2 + \left(\frac{\partial K}{\partial e}\right)^2} \ . \tag{6}$$

such that $s/K$ represents the estimate of the relative error in $K$ (and hence in $\rho_a$) per meter of uncertainty in $c$ and $e$. By neglecting the topography, $K$ and its partial derivatives can be calculated directly from Eq. 1. Therefore for these calculations we assume a flat surface at the average ground elevation across the transect. It should also be noted that, to be strictly correct, the values of $c$ and $e$ in Eq. 6 should be exact. The fact that they are uncertain by definition further reinforces the point that $s/K$ is an estimate. Nevertheless the following example suggests that $s/K$ provides a useful measure for identifying electrode configurations that are prone to geometric errors. We calculated $s/K$ for all 2,378 apparent resistivities, and removed any with an estimated relative error of $s/K \geq 5$ m$^{-1}$. This limit was chosen to reduce the systematic geometric errors to a level similar to that of the random noise. Since we estimated that the uncertainty in the array depths was ~1 cm, this limit equates to geometric errors of ~5 %, which is similar to the median level of reciprocal (random) error observed in the data. In total 342 apparent resistivities were removed by this process, leaving a data set comprising 2,036 measurements.

Figure 6(a) shows histograms comparing the distributions of apparent resistivity data before (black bars) and after (light gray bars) the data with high sensitivities to geometric error were filtered out. Note that the bin widths in the histogram are not uniform; this is so that we can depict in the same diagram the detailed distributions of the data before and after filtering. In the original data set, the apparent resistivities occurred in the range $-3{,}646\ \Omega\text{m} < \rho_a < 7{,}112\ \Omega\text{m}$. Since we expected the actual subsurface resistivities to lie approximately in the range $5\ \Omega\text{m} < \rho < 100\ \Omega\text{m}$, the presence of negative and large positive apparent resistivities makes it likely that some of the measurements were affected by geometric errors. Examining the distribution of the filtered data set strengthens this hypothesis. The range of apparent resistivities after filtering is $11\ \Omega\text{m} < \rho_a < 142\ \Omega\text{m}$, which seems more physically realistic. It is important to emphasize that none of the data were removed because of outlying resistivity values; they were filtered solely on the basis of the estimated sensitivity to geometric error, using limits set by the uncertainty in the electrode array depths and the degree of contamination by random noise. The fact that this technique has removed all the suspect data significantly increases our confidence in its use.

As demonstrated in Figs. (2) and (3), the geometric sensitivity of an electrode configuration depends on the geometric factor and its partial derivatives with respect to the positions of the electrodes. Large geometric sensitivities occur when $K$ changes rapidly with position, which will occur when $K$ is close to singular. Since $K$ will also be large in the vicinity of a singularity, it is reasonable to ask whether filtering by geometric sensitivity could be replaced with filtering by the geometric factor, which is simpler to calculate. Figure 6(b) shows a comparison of $s/K$ and $K$ for a specific configuration taken from panel 6 for which the in-hole electrode separations are $a = 0.8$ m, $b = 0.8$ m, the borehole separation is $d = 0.387$ m, and the midpoint depths are $c = 1.79$ m, $e = 1.27$ m. This configuration has a sensitivity of $s/K = 9.5\ \text{m}^{-1}$ and geometric factor of $|K| = 42.5$ m. In Fig. 6(b), $c$ is varied to demonstrate the behaviour of $s/K$ and $K$. Although both are large near the singularity, there is no one-to-one mapping between the two parameters, e.g. values of $s/K = 5\ \mathrm{m}^{-1}$ occur where $|K| = 63.8$ m on one side of the singularity and $|K| = 25.2$ m on the other. To reinforce this point, we removed 342 measurements with the largest $|K|$ from the full data set to compare with the results shown Fig. 6(a). Of the 342 measurements removed by $|K|$ filtering, 71 were different to those removed by $s/K$ filtering. After $|K|$ filtering, the resulting range of apparent resistivities was $-1\ \Omega\mathrm{m} < \rho_\mathrm{a} < 142\ \Omega\mathrm{m}$, which is not as realistic as that produced by filtering on $s/K$. A final question raised by filtering on $|K|$ is how to define the cut-off limit? In the above example, we chose to remove the same number of data as in Fig. 6(a), but without this prior information it seems that any upper limit on $|K|$ could only be assigned on an ad-hoc basis. By contrast, limits on geometric sensitivity can be determined directly from the known configuration geometry and estimates of the uncertainty in the electrode positions.

To investigate the benefits of removing the geometrically sensitive measurements, we inverted data from each individual panel and also the combined data set for the transect comprising all six panels. We used the Res2DInv software, with the finite-element method to permit the inclusion of topography, the complete Gauss-Newton solver, and $L_2$ model and data constraints (Loke *et al.*, 2003). The default settings were used for nearly all control parameters, which were kept identical for each inversion. However, the default damping factor was increased by a factor of two due to the high level of random noise in the data. In addition, the data were weighted using the difference between reciprocal measurements as an estimate of their random error. The systematic geometric errors were treated by filtering out configurations with high geometric sensitivity, which removed data from three of the panels. The inversions of the original and filtered data sets for these panels are compared in Fig. 7. For panel 1 (boreholes 44-45) 33 % of the data were removed; for panel 5 (boreholes 47-48) 6 % were removed; and for panel 6 (boreholes 49-50) 48 % were removed. Although the same measurement scheme (Fig. 5(a)) was used for each panel, the number of data that were removed from each is different. This is due to differences between the depths of the base electrodes in neighbouring boreholes, which changes the geometric factors and sensitivities of the electrode configurations from one panel to the next. For panels 1 and 6, removing the geometrically sensitive measurements significantly improved the RMS misfit between the inverted and observed apparent resistivities. For panel 5 there was almost no change, either in the inverted image or in the RMS misfit. But this is consistent with the estimated sensitivities of the data to geometric error. The small number of data that were removed from panel 5 had sensitivity estimates in the range $5.04\ \mathrm{m}^{-1} < s/K < 5.38\ \mathrm{m}^{-1}$, only just above the selected limit of $5\ \mathrm{m}^{-1}$. By contrast, the data that were removed from panels 1 and 6 had sensitivities of $5.01\ \mathrm{m}^{-1} < s/K < 1{,}020\ \mathrm{m}^{-1}$ and $8.67\ \mathrm{m}^{-1} < s/K < 1{,}380\ \mathrm{m}^{-1}$ respectively. Given that the data that were removed from panel 5 were consistent with the data that remained (since the RMS misfit was unchanged), whilst the data that were removed from panels 1 and 6 were not (since the RMS misfits significantly decreased), this provides further evidence that $s/K$ is a useful estimate of the sensitivity to geometric error.

Having assessed the individual panels, in Fig. 8 we compare the inverted images of the data set before (a) and after (b) filtering for the entire six-panel transect. Both images exhibit regions of low resistivity within ~0.05 m of each vertical electrode array, which is consistent with a borehole of 100 mm diameter filled with water and poorly consolidated material from collapsed borehole walls. Between the boreholes, the resistivities are somewhat higher than the expected values shown in Fig. 4. This may be due to compaction by the sonic percussion drilling method. Nevertheless, the images do seem to show four distinct layers that correspond quite closely with the lithostratigraphic section in Fig. 4. The interfaces between the strata are shown by dotted lines overlaid on Fig. 8(a). In both images, there appears to be a fairly low contrast boundary at a depth of ~1.5 m that corresponds well with the first interface. Another more obvious, higher contrast boundary occurs at ~3 m, which is about 0.1 m - 0.2 m above the second interface. The highest contrast boundary exists at ~5.8 m, which probably corresponds to the third interface, although this is about 0.5 m below. We note again however that the lithostratigraphic interfaces are approximate, having been interpolated from boreholes adjacent to the test site. For clarity we have plotted our observed boundaries on Fig. 8(b) only (dashed lines), although they apply equally well to both images. They partition each image into four regions (I, II, III, and IV), and the average resistivities in each region are shown. It should be noted that in all four regions the material was highly disturbed by the drilling and the installation of the multi-level sampler completions. There may also have been localized differences in the vertical distribution of chloride resulting from the reductive dechlorination process. Both of these considerations make an exact correlation between the inverted image and nearby cone penetrometer resistivity profiles unlikely. In region I, the average resistivity is much lower than expected (~20 Ωm compared to ~100 Ωm). This is probably because there were several electrodes in the resistive vadose zone that failed to make good galvanic contact and were not used. Therefore most data in region I were measured in the less resistive saturated zone of the made ground. For region II, the resistivity is significantly higher than expected (~30 Ωm instead of ~5 Ωm), but the exact reasons for this discrepancy are not clear. In region III, the average resistivity of ~60 Ωm is in reasonable agreement with the expected value of ~20 Ωm - 50 Ωm. At the base of the image (region IV), the resistivity is somewhat higher than expected (~20 Ωm compared to ~10 Ωm), but the lack of agreement is probably due to low data density since only ~10 % of the electrodes were in this region.

The qualitative differences between Figs. 8(a) and 8(b) are not as obvious as for some of the individual panels. This is because no data were removed from three of the panels (2, 3 and 4). The unchanged data from these panels have an influence on the inverted image in adjacent panels (Maurer & Friedel 2006), which tends to ensure consistency of the image across the entire transect. Figure 9(a) shows a quantitative comparison in terms of the logarithm of the ratio of the model resistivities before and after filtering. This shows that the changes occur predominantly in panel 6, and to a lesser extent in panel 1, which is consistent with the numbers of measurements that were removed from each. As noted above, the influence of data on adjacent panels is the likely cause of the resistivity changes in panel 2, and is probably largely responsible for the changes in panel 5, given that the small number of data removed from this panel had little effect on its individual inverted image (see Fig 7(b)). It is not possible to associate specific localised resistivity changes with the removal of individual measurements, since the data tend to be filtered out in groups that are distributed evenly along the vertical extent of each affected panel. This is illustrated in Fig. 9(b) which indicates the configurations that were removed from panel 5. The reason for the removal of all configurations with a particular fixed geometry over a range of depths is that the geometric factor and its derivatives depend only weakly on the depth of the configuration below the surface.

In resistivity inversion, it is normally desirable to use the logarithm of the apparent resistivity as the data parameter. This transforms the typically large range of resistivity values to a linear scale and ensures that all the data have equal weight irrespective of their magnitude. But it is worth noting that the full data set, including measurements with negative apparent resistivities, can be inverted without filtering if a different data parameter is used. Table 2 shows the RMS misfit obtained for the full and filtered data sets using the resistance, the apparent resistivity, and the logarithm of the apparent resistivity as the data parameters. In each case, the inversion was terminated when the relative change in the RMS misfit was <0.1 %. It is clear from Table 2 that removing geometrically sensitive measurements is beneficial whichever data parameter is used. But the advantage of geometric sensitivity filtering is that it will extract a subset of measurements that can be inverted using the logarithmic data parameter. Of the three that were tested, this parameter produced the lowest value of the RMS misfit in the above example (4.8 %), significantly improving on the quality of the fit obtained before filtering. This misfit is consistent with the level of random noise in the data, which strongly suggests that the systematic geometric errors have been suppressed effectively by this approach.

| Data set | Resistance | Apparent Resistivity | Log Apparent Resistivity |
|---|---|---|---|
| Full | 10.3 % | 11.1 % | - |
| Filtered | 6.9 % | 5.7 % | 4.8 % |

**TABLE 2: RMS misfit errors obtained using the specified data parameters.**

# 6. Conclusions

Since data errors caused by uncertainties in the geometry of borehole ERT configurations are systematic in nature, they will not directly be accounted for by weighting or filtering based on the reciprocal error. Therefore it is important to obtain other estimates of their effects on the measured data. We have shown how to derive analytical expressions for the sensitivity of such measurements to geometric error, which can be applied to configurations with any number of electrodes from pole-pole upwards. The sensitivity, which is calculated from the geometric factor for a homogeneous half-space, is an estimate since the exact geometry of the measurement configuration and the resistivity distribution of the subsurface are unknown.

We have studied the behaviour of the geometric sensitivity for two generic four-electrode configurations that are frequently used in borehole ERT: IH (current flow and potential difference in-hole) and XH (current flow and potential difference crosshole). Using dimensionless distance units for generality, our results show that some IH configurations possess high sensitivity to geometric error for *any* separation between the boreholes. By contrast, XH configurations are affected to a much lesser degree, only exhibiting high sensitivities for small borehole separations (typically less than the vertical spacing of the current and potential electrodes in the same hole). Since XH configurations also provide superior image resolution and signal-to-noise characteristics, this additional advantage strengthens the case for their use in preference to the IH type.

To demonstrate the usefulness of this approach, we applied it to estimate the sensitivities of all the measurement configurations that were used to gather test data from a newly installed transect of closely spaced boreholes. This transect is part of an ongoing research program to monitor bioremediation of chlorinated solvents at a contaminated industrial site. The electrode arrays were installed on rigid plastic tubing with precise and constant inter-electrode spacings of 20 cm. However, the estimated uncertainty in the depths of installation of each array was ~1 cm. Although only XH configurations were used, the small separations between the boreholes (~45 cm) caused some configurations to be highly sensitive to geometric error. Using the estimated sensitivity to geometrical error and the uncertainty in the array depth, we filtered out 14 % of the data that had estimated systematic errors, caused by uncertain array geometries, of ≥5 %. Without referring to the measured data in any way, this process removed *all* the outlying measurements with physically unrealistic apparent resistivities. This enabled the use of logarithmic data which tends to improve the stability of the inversions. The results showed a marked improvement in convergence between the inverted and measured data, both for individual borehole pairs and for the whole transect.

The calculations involved in estimating the sensitivity of borehole ERT measurements to geometric error are straightforward and easy to implement. It may be possible to combine the estimates of geometric error with those obtained from the data for random noise, and subsequently use the combined error to weight the data in the inversion. However, our results show that simply filtering apparent resistivity measurements using this estimate can significantly improve the fit between the observed and the inverted data.

## Acknowledgements

Project SABRE is being undertaken by a collaborative team comprising: Acetate Products; Archon Environmental; British Geological Survey; Chevron; CL:AIRE; DuPont; Environment Agency (England and Wales), ESI; General Electric; GeoSyntec; Golder Associates; Honeywell; ICI; Scientifics; SiREM; Shell; Terra Systems; University of Edinburgh; University of Sheffield; US EPA. SABRE is a UK DTI Bioremediation LINK project with specific funding contributions made by BBSRC, DTI, the Environment Agency, EPSRC and NERC. Additional funding has been provided by SERDP (US Department of Defense). The SABRE team gratefully acknowledges these supporting organizations and the in-kind and direct financial contributions made by each team member.

We thank the editor (Dr. Oliver Ritter) and two anonymous reviewers for their helpful comments on our original manuscript. This paper is published with permission of the Executive Director of the British Geological Survey (NERC).

# References

Bing, Z. & Greenhalgh, S.A., 2000. Cross-hole resistivity tomography using different electrode configurations, *Geophysical Prospecting*, **48**, 887-912.

Blott, B.H., Daniell, G.J. & Meeson, S., 1998. Electrical impedance tomography with compensation for electrode positioning variations, *Physics in Medicine and Biology*, **43**, 1731-1739.

Carpenter, E.W. & Habberjam, G.M., 1956. A tri-potential method of resistivity prospecting, *Geophysics*, **11**, 455-469.

Chambers, J.E., Wilkinson, P.B., Weller, A.L., Meldrum, P.I., Ogilvy, R.D. & Caunt, S., 2007. Mineshaft imaging using surface and crosshole 3D electrical resistivity tomography: a case history from the East Pennine Coalfield, UK, *Journal of Applied Geophysics*, **62**, 324-337.

Cho, I.-K., Kim, J.-H., Chung, S.-H. & Suh, J.-H., 2002. Negative apparent resistivity in resistivity method, *Mulli-Tamsa (Geophysical Exploration)*, **5**, 199-205.

Daily, W. & Ramirez, A.L., 2000. Electrical imaging of engineered hydraulic barriers, *Geophysics*, **65**, 83-94.

Goes, B.J.M. & Meekes, J.A.C., 2004. An effective electrode configuration for the detection of DNAPLs with electrical resistivity tomography, *Journal of Environmental and Engineering Geophysics*, **9**, 127-141.

Keller, G.V. & Frischknecht, F.C., 1966. *Electrical methods in geophysical prospecting*, Pergamon Press, Oxford.

Kumar, R., 1973. Resistivity type curves over outcropping vertical dyke-I, *Geophysical Prospecting*, **21**, 560.

Ogilvy, R.D., Kuras, O., Meldrum, P.I., Wilkinson, P.B., Gisbert, J., Jorreto, S., Pulido Bosch, A., Kemna, A., Nguyen, F. & Tsourlos, P., 2007. Automated monitoring of coastal aquifers with electrical resistivity tomography. *In: A. Pulido Bosch, J.A. López-Geta and G. Ramos González (Editors), Coastal Aquifers: Challenges and Solutions.* Hidrogeología y aguas subterraneas; nº 23. Instituto Geológico y Minero de España, Madrid, 333-342.

LaBrecque, D.J., Milleto, M., Daily, W., Ramirez, A. & Owen, E., 1996. The effects of noise on Occam's inversion of resistivity tomography data, *Geophysics*, **61**, 538-548.

LaBrecque, D.J., Heath, G., Sharpe, R. & Versteeg, R., 2004. Autonomous monitoring of fluid movement using 3-D electrical resistivity tomography, *Journal of Environmental and Engineering Geophysics*, **9**, 167-176.

Loke, M.H. & Barker, R.D., 1995. Least-squares deconvolution of apparent resistivity pseudosections, *Geophysics*, **60**, 1682-1690.

Loke, M.H., Acworth, I. & Dahlin, T., 2003. A comparison of smooth and blocky inversion methods in 2-D electrical imaging surveys, *Exploration Geophysics*, **34**, 182–187.

Maurer, H. & Friedel, S., 2006. Outer-space sensitivities in geoelectrical tomography, *Geophysics*, **71**, G93-G96.

Oldenborger, G.A., Routh, P.S. & Knoll, M.D., 2005. Sensitivity of electrical resistivity tomography data to electrode position errors, *Geophysical Journal International*, **163**, 1-9.

Parasnis, D.S., 1966. *Mining Geophysics*, Elsevier Publishing, London.

Parasnis, D.S., 1988. Reciprocity theorems in geoelectric and geoelectromagnetic work, *Geoexploration*, **25**, 177-198.

Ramirez, A., Daily, W., Binley, A., LaBrecque, D. & Roelant D., 1996. Detection of leaks in underground storage tanks using electrical resistance methods, *Journal of Environmental and Engineering Geophysics*, **1**, 189-203.

Ridd, P.V., 1994. Electric potential due to a ring electrode, *IEEE Journal of Oceanic Engineering*, **19**, 464-467.

Soleimani, M., Gomez-Laberge, C. & Adler, A., 2006. Imaging of conductivity changes and electrode movement in EIT, *Physiological Measurement*, **27**, S103-S113.

Slater, L., Binley, A., Versteeg, R., Cassiani, G., Birken, R. & Sandberg, S., 2002. A 3D ERT study of solute transport in a large experimental tank, *Journal of Applied Geophysics*, **49**, 211-229.

Slater, L. & A. Binley, 2003. Evaluation of permeable reactive barrier (PRB) integrity using electrical imaging methods, *Geophysics*, **68**, 911-921.

Versteeg, R., Ankeny, M., Harbour, J., Heath, G., Kostelnik, K., Mattson, E., Moor, K., Richardson, A. & Wangerud, K., 2004. A structured approach to the use of near-surface geophysics in long-term monitoring, *The Leading Edge*, **23**, 700-703

Wilkinson, P.B., Chambers, J.E., Meldrum, P.I., Ogilvy, R.D. & S. Caunt, 2006. Optimization of array configurations and panel combinations for the detection and imaging of abandoned mineshafts using 3D cross-hole electrical resistivity tomography, *Journal of Environmental and Engineering Geophysics*, **11**, 213-221.

Zhang, J. & Patterson, R.P., 2005. EIT images of ventilation: what contributes to the resistivity changes?, *Physiological Measurement*, **26**, S81-S92.

Zhou, B. & Dahlin, T., 2003. Properties and effects of measurement errors on 2D resistivity imaging surveying, *Near Surface Geophysics*, **1**, 105-117.

# Figure Captions

**Figure 1.** Geometry of (a) crosshole (XH) and (b) in-hole (IH) arrays for evaluation of general electrode position errors, and (c) XH and (d) IH arrays for evaluation of depth offset errors between adjacent boreholes. Current and potential electrodes are shown as open and filled circles respectively. Distances in (c) and (d) are given as multiples of the vertical electrode separation $a$.

**Figure 2.** Surface and line plots of (a) error estimate $\sigma$, (b) inverse of the geometric factor $1/K$, and (c) relative error estimate $\sigma/K$ for XH configurations. In all plots, the left-hand midpoint depth is fixed at $\gamma = 10$, and the right-hand midpoint depth range is $5 \leq \varepsilon \leq 15$. In the surface plots, the range of borehole separations is $0.5 \leq \delta \leq 5$.

**Figure 3.** Surface and line plots of (a) error estimate $\sigma$, (b) inverse of the geometric factor $1/K$, and (c) relative error estimate $\sigma/K$ for IH configurations. In all plots, the left-hand midpoint depth is fixed at $\gamma = 10$, and the right-hand midpoint depth range is $5 \leq \varepsilon \leq 15$. In the surface plots, the range of borehole separations is $0.5 \leq \delta \leq 5$.

**Figure 4.** Plan view of SABRE test cell, showing source and plume zone transect borehole fences. The lithostratigraphic section shows the expected resistivities of the four strata and the depths of the seven boreholes on the source zone transect.

**Figure 5.** (a) XH multi-channel measurement scheme used to collect ERT data on each panel. The dashed line joins the current electrodes, the dotted lines join sequential pairs of potential electrodes. (b) Geometry for evaluation of depth offset errors between adjacent boreholes for general XH arrays.

**Figure 6.** (a) Distribution of apparent resistivities before and after filtering out measurements with high sensitivity to geometric error (black and gray bars respectively). (b) Comparison of the geometric sensitivity ($s/K$) and geometric factor ($K$) with midpoint depth $c$ for a specific four-electrode configuration. The shaded region indicates the region for which $s/K > 5$ m$^{-1}$, and the arrow indicates the actual midpoint depth and sensitivity of the given measurement.

**Figure 7.** Comparison of ERT images before and after filtering for (a) panel 1, (b) panel 5, and (c) panel 6. The RMS misfits ($E_{\mathrm{rms}}$) are given beneath each image.

**Figure 8.** Comparison of ERT images for the entire transect (a) before and (b) after filtering. The RMS misfit ($E_{\mathrm{rms}}$) and average resistivities for regions I-IV are given beneath each image. Predicted lithostratigraphic interfaces are shown as dotted lines in (a), observed interfaces are shown as dashed lines in (b).

**Figure 9.** (a) Logarithm of the ratio of the model resistivities before and after filtering. (b) Illustration of the shallowest and deepest configurations that were removed from panel 5 by geometric sensitivity filtering. The current and potential bipoles are shown by red and blue lines respectively. The arrow indicates that all

configurations with the same fixed geometry lying between these two were also removed from panel 5.

**Figure A1.** (a) Geometry of a XH configuration with a large and close to singular geometric factor. The subsurface resistivity distribution is a vertically faulted half-space, with resistivities $\rho_1$ and $\rho_2$. (b) Dependence of apparent resistivity $\rho_a$ on $\rho_2$.

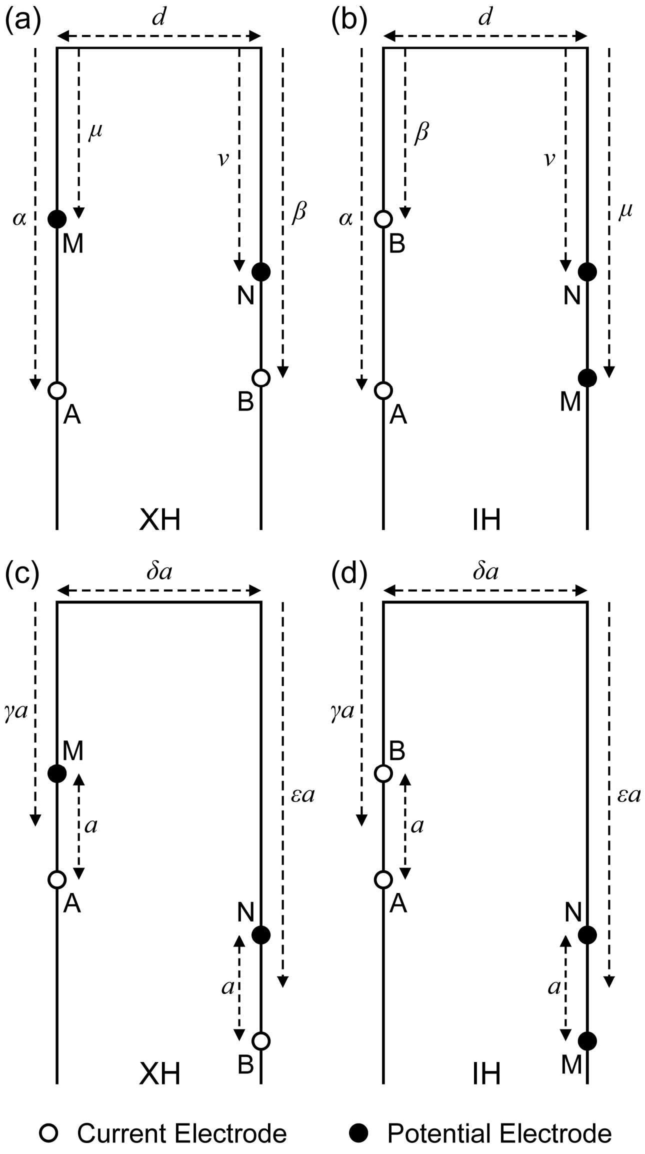
(a)
d
μ
v
α
β
M
N
A
B
XH
(b)
d
β
v
α
μ
B
N
A
M
IH
(c)
δa
γa
M
a
A
εa
N
a
B
XH
(d)
δa
γa
B
a
A
εa
N
a
M
IH
○ Current Electrode
● Potential Electrode

**Figure 1**

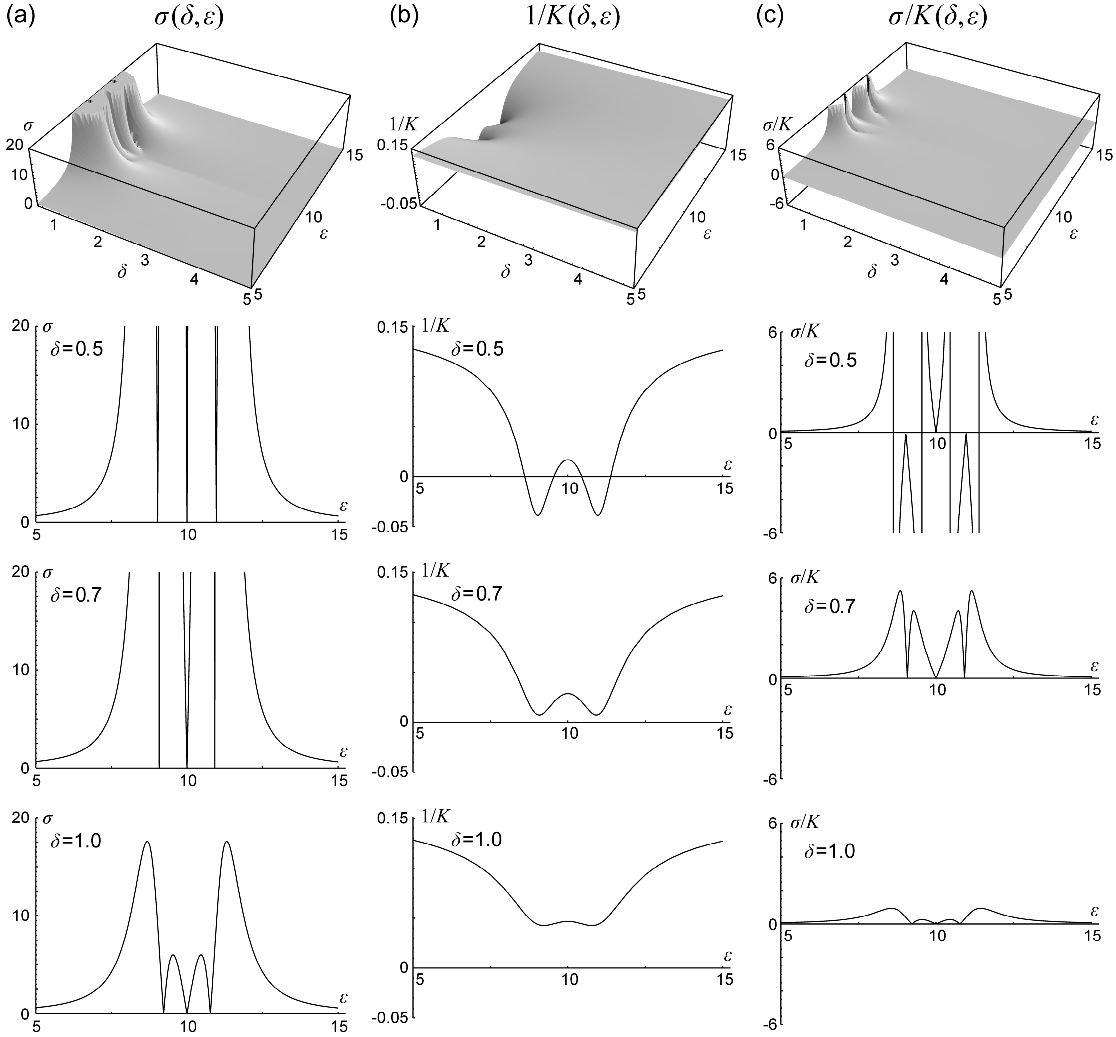
(a)
σ(δ,ε)
(b)
1/K(δ,ε)
(c)
σ/K(δ,ε)
σ
1/K
σ/K
δ
ε
δ=0.5
δ=0.7
δ=1.0
20
10
0
0.15
-0.05
6
-6
1
2
3
4
5
10
15

**Figure 2**

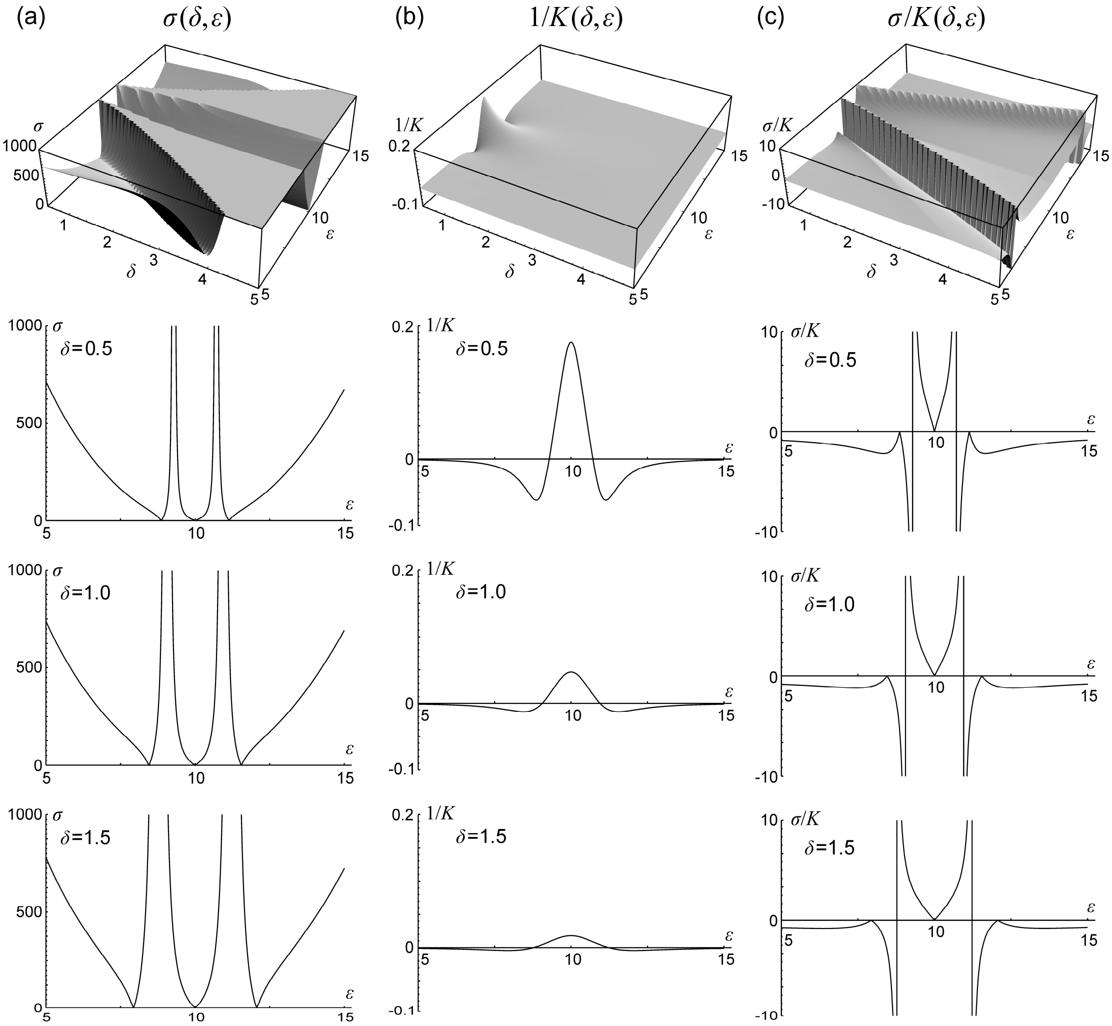

(a)
σ(δ,ε)
(b)
1/K(δ,ε)
(c)
σ/K(δ,ε)
σ
1000
500
0
1
2
3
4
5
δ
5
10
15
ε
1/K
0.2
-0.1
σ/K
10
0
-10
δ=0.5
δ=1.0
δ=1.5

**Figure 3**

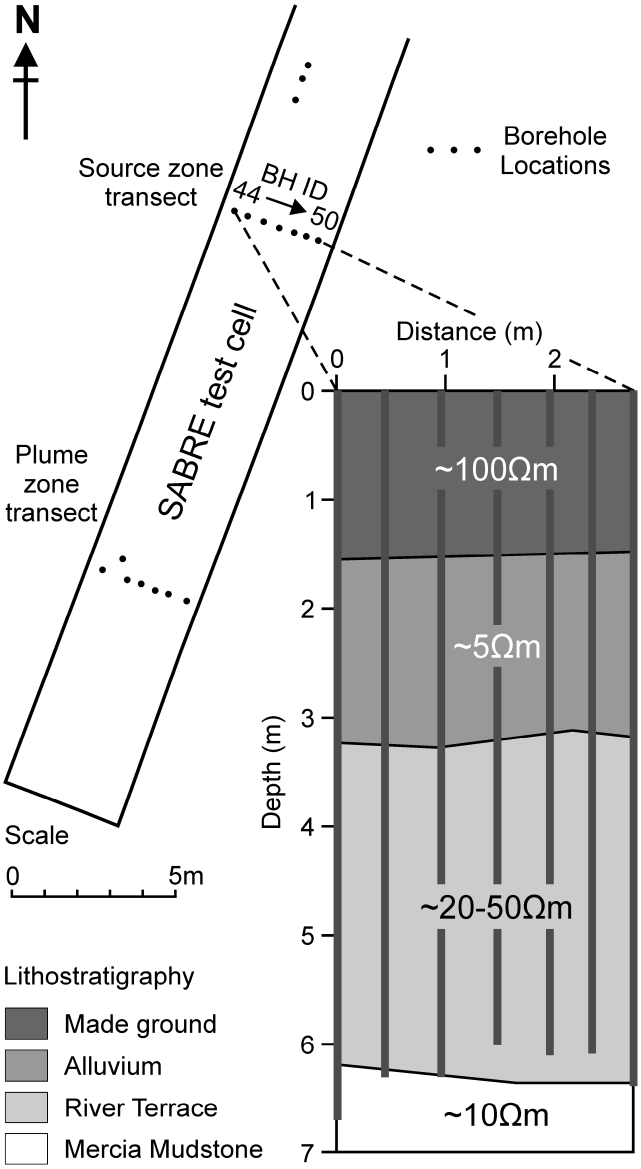
N
Source zone transect
BH ID
44
50
Borehole Locations
SABRE test cell
Plume zone transect
Scale
0
5m
Distance (m)
0
1
2
Depth (m)
0
1
2
3
4
5
6
7
~100Ωm
~5Ωm
~20-50Ωm
~10Ωm
Lithostratigraphy
Made ground
Alluvium
River Terrace
Mercia Mudstone

**Figure 4**

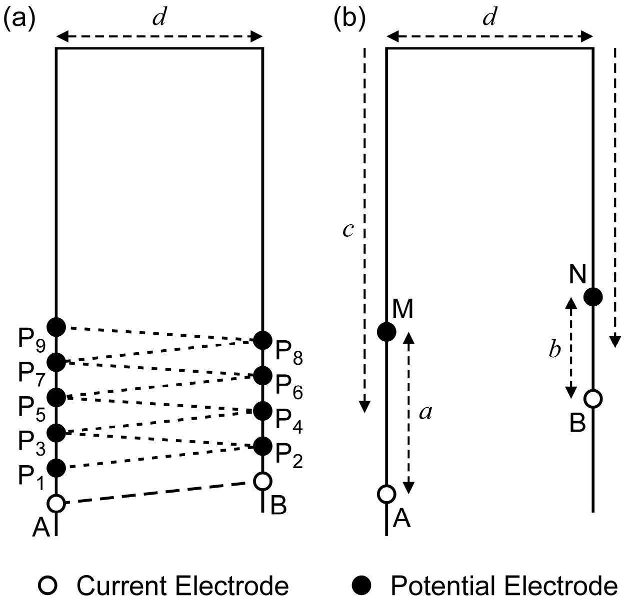
(a)
d
P9
P7
P5
P3
P1
A
P8
P6
P4
P2
B
(b)
d
c
e
N
M
b
a
B
A
○ Current Electrode
● Potential Electrode

**Figure 5**

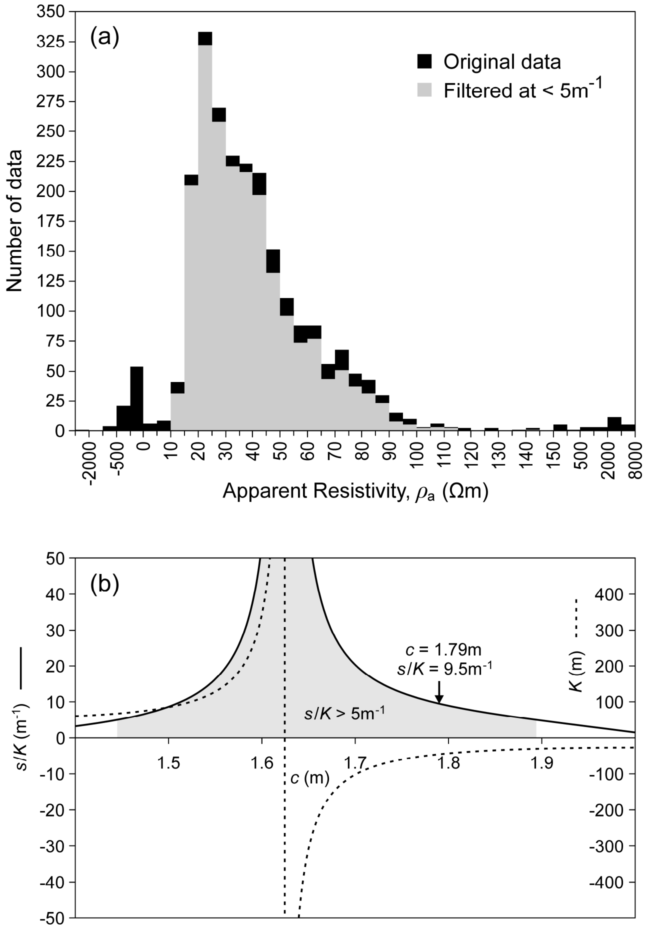
(a)
Original data
Filtered at < 5m$^{-1}$
Number of data
0
25
50
75
100
125
150
175
200
225
250
275
300
325
350
-2000
-500
0
10
20
30
40
50
60
70
80
90
100
110
120
130
140
150
500
2000
8000
Apparent Resistivity, $\rho_a$ (Ωm)
(b)
$s/K$ (m$^{-1}$)
$K$ (m)
50
40
30
20
10
0
-10
-20
-30
-40
-50
400
300
200
100
-100
-200
-300
-400
1.5
1.6
1.7
1.8
1.9
$c$ (m)
$c$ = 1.79m
$s/K$ = 9.5m$^{-1}$
$s/K$ > 5m$^{-1}$

**Figure 6**

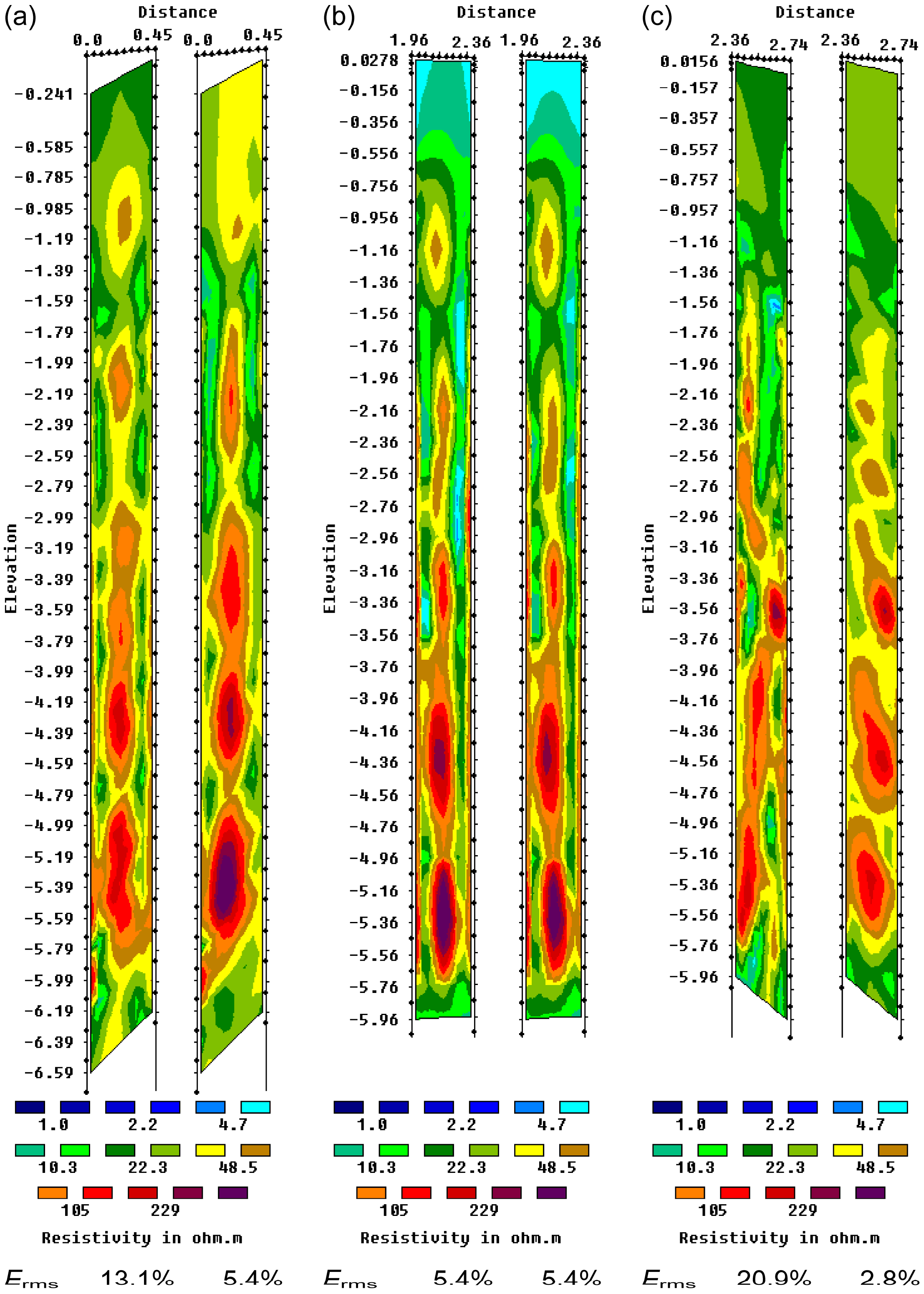(a)
Distance
0.0
0.45
0.0
0.45
Elevation
-0.241
-0.585
-0.785
-0.985
-1.19
-1.39
-1.59
-1.79
-1.99
-2.19
-2.39
-2.59
-2.79
-2.99
-3.19
-3.39
-3.59
-3.79
-3.99
-4.19
-4.39
-4.59
-4.79
-4.99
-5.19
-5.39
-5.59
-5.79
-5.99
-6.19
-6.39
-6.59
1.0
2.2
4.7
10.3
22.3
48.5
105
229
Resistivity in ohm.m
$E_{rms}$
13.1%
5.4%
(b)
Distance
1.96
2.36
1.96
2.36
Elevation
0.0278
-0.156
-0.356
-0.556
-0.756
-0.956
-1.16
-1.36
-1.56
-1.76
-1.96
-2.16
-2.36
-2.56
-2.76
-2.96
-3.16
-3.36
-3.56
-3.76
-3.96
-4.16
-4.36
-4.56
-4.76
-4.96
-5.16
-5.36
-5.56
-5.76
-5.96
1.0
2.2
4.7
10.3
22.3
48.5
105
229
Resistivity in ohm.m
$E_{rms}$
5.4%
5.4%
(c)
Distance
2.36
2.74
2.36
2.74
Elevation
0.0156
-0.157
-0.357
-0.557
-0.757
-0.957
-1.16
-1.36
-1.56
-1.76
-1.96
-2.16
-2.36
-2.56
-2.76
-2.96
-3.16
-3.36
-3.56
-3.76
-3.96
-4.16
-4.36
-4.56
-4.76
-4.96
-5.16
-5.36
-5.56
-5.76
-5.96
1.0
2.2
4.7
10.3
22.3
48.5
105
229
Resistivity in ohm.m
$E_{rms}$
20.9%
2.8%

**Figure 7**

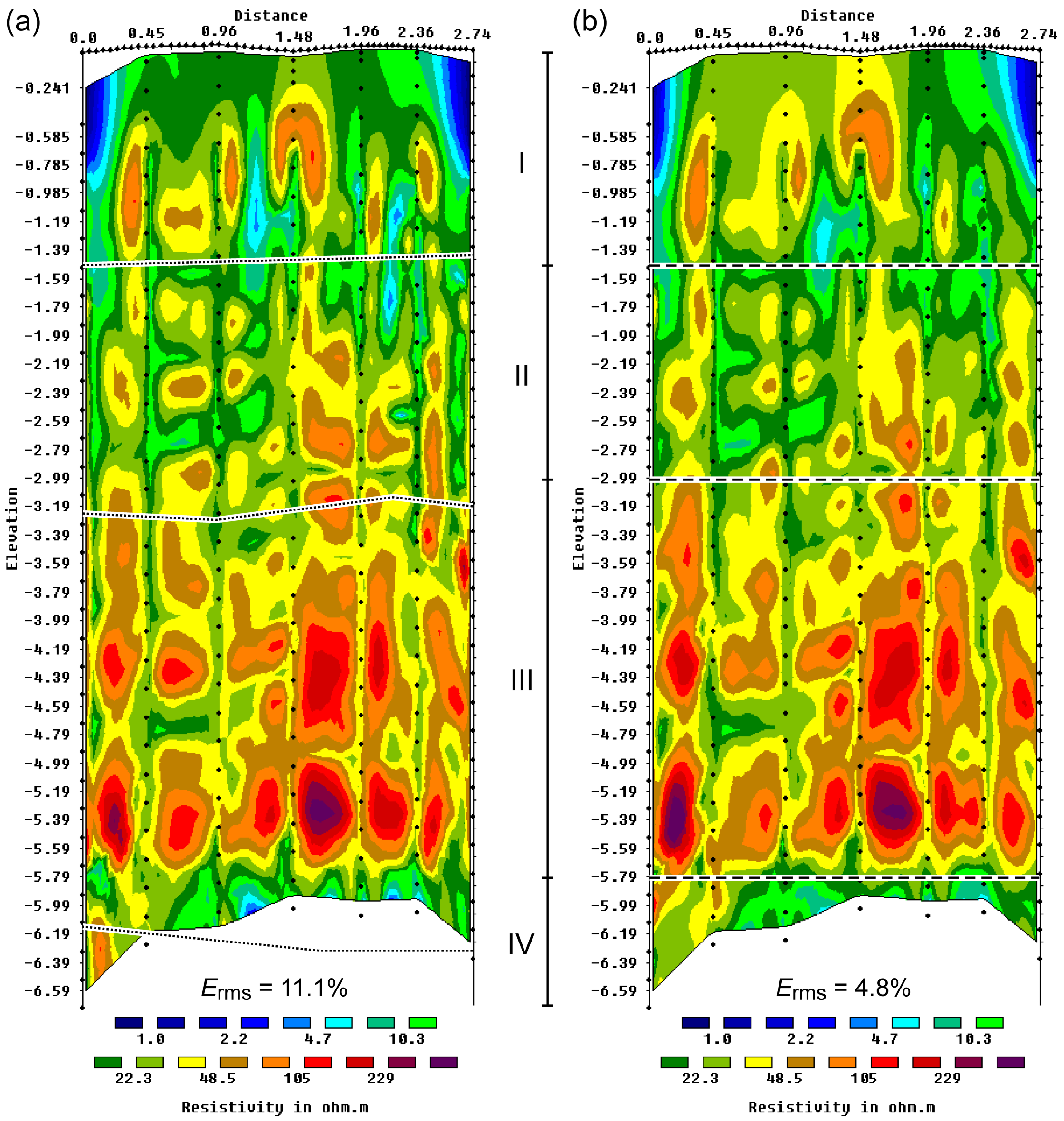

$\overline{\rho}_{I} = 22\Omega m$ $\overline{\rho}_{II} = 28\Omega m$

$\overline{\rho}_{III} = 60\Omega m$ $\overline{\rho}_{IV} = 21\Omega m$

$\overline{\rho}_{I} = 24\Omega m$ $\overline{\rho}_{II} = 28\Omega m$

$\overline{\rho}_{III} = 63\Omega m$ $\overline{\rho}_{IV} = 22\Omega m$

**Figure 8**

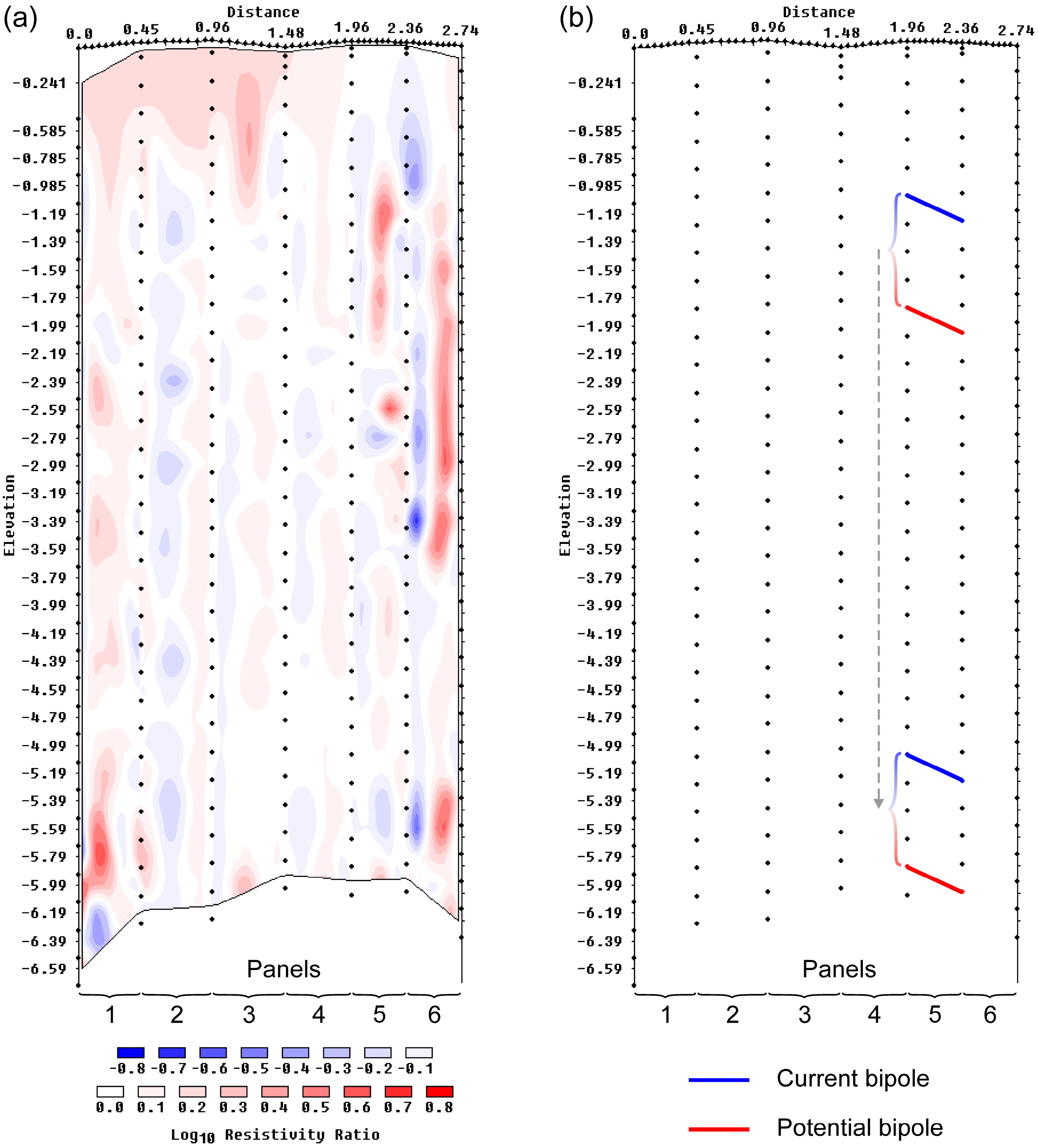
(a)
Distance
0.0
0.45
0.96
1.48
1.96
2.36
2.74
Elevation
-0.241
-0.585
-0.785
-0.985
-1.19
-1.39
-1.59
-1.79
-1.99
-2.19
-2.39
-2.59
-2.79
-2.99
-3.19
-3.39
-3.59
-3.79
-3.99
-4.19
-4.39
-4.59
-4.79
-4.99
-5.19
-5.39
-5.59
-5.79
-5.99
-6.19
-6.39
-6.59
Panels
1
2
3
4
5
6
-0.8 -0.7 -0.6 -0.5 -0.4 -0.3 -0.2 -0.1
0.0 0.1 0.2 0.3 0.4 0.5 0.6 0.7 0.8
Log10 Resistivity Ratio
(b)
Current bipole
Potential bipole

**Figure 9**

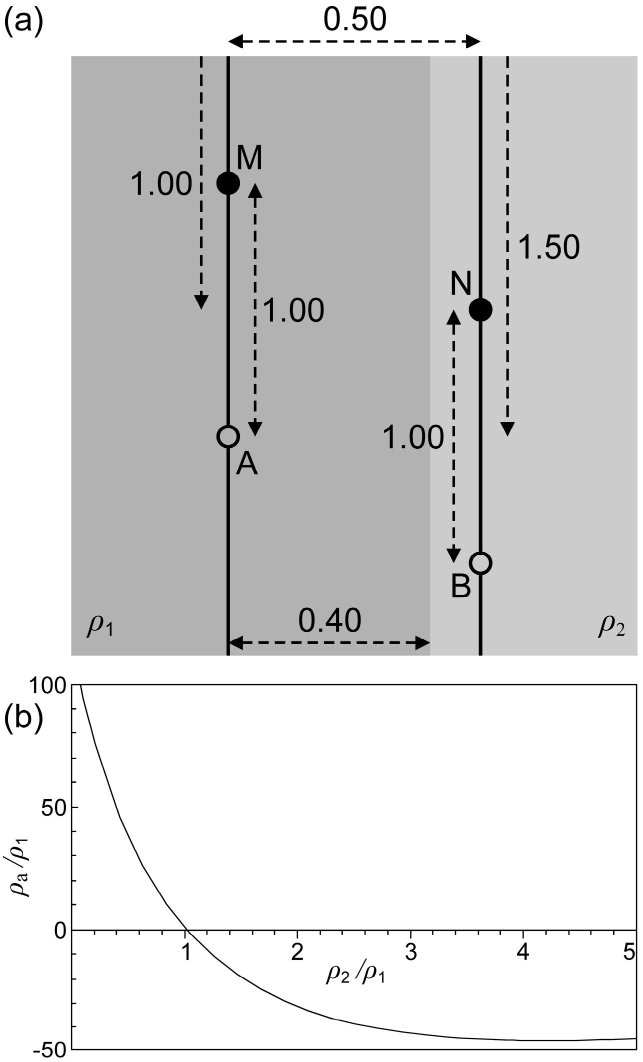

**Figure A1**

# Appendix A: The reality of negative apparent resistivities

The apparent resistivity $\rho_a$ is often described as a weighted average of the resistivity distribution through which the current flows, despite the fact that this has long been known to be wrong (Parasnis 1966). More correctly, it can be understood as the resistivity of a hypothetical homogeneous subsurface that would yield the same potential difference when using the same current and arrangement of electrodes. But in either interpretation, it is very difficult to understand the physical meaning of negative apparent resistivities. In our experience, they are often attributed to noise, or to the current or voltage electrodes being accidentally transposed. But it is not always the case that a negative apparent resistivity is an indicator of random or systematic error. There are circumstances under which $\rho_a < 0$ is possible, and is a valid measurement. This was first pointed out by Carpenter & Habberjam (1956) for a layered earth, by Kumar (1973) for an outcropping vertical dyke, and has been recently rediscovered by Cho *et al.* (2002) and by ourselves.

Let $\mathbf{E}_i$ be the electric field in the vicinity of the potential electrodes M and N in the inhomogeneous half-space in which we are measuring the apparent resistivity. Similarly, let $\mathbf{E}_h$ be the electric field in the same region of a homogeneous half-space with the same electrode configuration. Also, let $\mathbf{r}_{MN}$ be the vector from M to N. If $\rho_a < 0$ it implies that the component of $\mathbf{E}_i$ along $\mathbf{r}_{MN}$ points in the *opposite direction* to the same component of $\mathbf{E}_h$. This can happen if the secondary field in the vicinity of M and N, which is caused by the inhomogeneous resistivity distribution, is greater than the primary field, which is due to the current electrodes (Cho *et al.*, 2002). This is not often the case, but it can happen if the primary field is weak (i.e. the potential difference is small, which occurs if the geometric factor is close to singular), and if there are strong resistivity contrasts near the electrodes (so that the weak primary fields are distorted by strong secondary fields).

Since geoelectrical inversion algorithms usually regard the electrode positions as fixed and accurate, what happens if a geometric error significantly changes an apparent resistivity measurement, or causes it to become negative? If $\rho_{\mathrm{a}}$ increases then the volumetric average concept suggests that localized high contrast anomalies will appear in the resistivity tomogram near the affected electrodes, increasing the apparent resistivity of that particular measurement. But if $\rho_{\mathrm{a}}$ becomes negative then this interpretation is not valid. In this case, we must consider the problem in terms of strong secondary fields. This also suggests that high contrast anomalies are likely to appear near the electrodes. These anomalies would distort the primary field, and if strong enough, could cause the predicted apparent resistivity to become negative and therefore improve the fit to the observed data that are negative due to geometric error. Figure A1 demonstrates a simple example of a real negative apparent resistivity measured using a XH configuration and caused by a resistivity contrast close to two of the electrodes. In Fig. A1a, the XH configuration is close to singular, and has a high geometric factor of $K \approx 5{,}700\ \mathrm{m}$. The resistivity distribution is a vertically faulted half space, with $\rho = \rho_1$ to the left of the fault, and $\rho = \rho_2$ to the right. The apparent resistivity for this configuration can be calculated easily by incorporating image charges above the surface into the standard solution for the surface potential (Keller & Frischknecht 1966). The variation of $\rho_a$ as a function of the resistivity contrast is shown in Fig. A1b. This demonstrates that the apparent resistivity can change dramatically with the contrast across the fault, and can indeed become negative. Since $\rho_a > \rho_1$ when $\rho_2 < \rho_1$, and $\rho_a < \rho_1$ when $\rho_2 > \rho_1$, there are no circumstances in this example for which $\rho_a$ can be a weighted average of $\rho_1$ and $\rho_2$. This is true whether $\rho_a$ is positive or negative.